Effect of transition dipole phase on high-order-harmonic generation in solid materials

Shicheng Jiang, Hui Wei, Jigen Chen, Chao Yu, Ruifeng Lu, and C. D. Lin

Effect of transition dipole phase on high-order harmonic generation in solid materials

Shicheng Jiang[1,2], Hui Wei[2], Jigen Chen[2,3], Chao Yu[1], Ruifeng Lu[1,4,†] and C. D. Lin[2,*]

[1] Department of Applied Physics, Nanjing University of Science and Technology, Nanjing 210094, P. R. China
[2] J. R. Macdonald Laboratory, Department of Physics,
Kansas State University, Manhattan, Kansas 66506, USA
[3] Department of Physics, Taizhou University, Taizhou 318000, P. R. China and
[4] State Key Laboratory of Molecular Reaction Dynamics, Dalian Institute of Chemical Physics,
Chinese Academy of Sciences, Dalian 116023, P. R. China*

High-order harmonic spectra from solid materials driven by single-color multicycle laser fields sometimes contain even harmonics. In this work we attribute the appearance of even harmonics to the non-zero transition dipole phase (TDP) when the solid system has broken symmetry. By calculating the harmonic efficiency from graphene and gapped graphene using the semiconductor Bloch equations under the tight-binding approximation, we demonstrate the role of TDP which has been ignored for a long time. When the crystal has inversion symmetry, or reflection symmetry with the symmetry plane perpendicular to the laser polarization direction, the TDP can be neglected. Without such symmetry, however, the TDP will lead to the appearance of even harmonics. We further show that TDP is sensitive to the crystal geometry. To extract the structure information from the harmonic spectra of a solid the TDP cannot be ignored.

I. INTRODUCTION

Since the first observation of non-perturbative high-order harmonic generation (HHG) in ZnO crystal in 2011 [1], HHG from solid materials has been reported by various experimental groups. It has been demonstrated that efficient harmonic emission can be achieved from solid materials than from atoms and molecules [2] because of the high density and the periodic structure in the crystal. The HHG plateau in crystals has been extended to the EUV region recently [3, 4] and it may become potential sources of attosecond pulse generation. The highly nonlinear interaction between femtosecond lasers and crystals also paves the way for controlling the electric current in solids into the petahertz domain [5, 6]. This means that the maximum processor speed can exceed the limit imposed by the traditional metal-oxide-semiconductor field-effect transistors (MOSFETs) in the future. It has also been proposed that HHG from solids can be used for an all-optical reconstruction of the band structure[7–9] and spatial structure [10].

In order to implement such possible applications, an accurate physical model that can describe the mechanism of HHG from solid materials is needed. To date, there are three main theoretical approaches for the study of the HHG process from solids: the Wannier-Bloch approach using localized Wannier wave functions for valence band and delocalized Bloch functions for conduction band[11], the time-dependent Schrödinger equation (TDSE) and semiconductor Bloch equations (SBEs) approaches using the Bloch basis functions under the single-electron approximation [12, 13], and time-dependent density functional theory (TDDFT) by solving the time-dependent Kohn-Sham equations [14–16]. Since the band theory

gives a direct access to the crystal structure, the TDSE and SBEs based on the Bloch basis functions were widely used in recent years. We show later that SBEs can be derived from TDSE where the dephasing effect in solids can be introduced[17–19]. Using the Bloch picture, there are two major mechanisms that contribute to the HHG process: the intraband current and the interband polarization. These two mechanisms have been used to interpret many experimental results successfully [1, 3, 9, 10, 20–23]. Generally speaking, both mechanisms strongly depend on the band structure [1, 3] of the solid and the nature of its transition dipole moment [24]. However, it is not clear whether one mechanism dominates the other in a given experiment without the analysis of the calculation.

In solids, angular dependent HHG spectra have been reported in many experiments [1, 10, 20, 23, 25–27]. While in certain laser polarization directions only odd harmonics were observed, in other directions even harmonics also appeared. Based on simple physical picture, the appearance of even-order harmonics can be easily understood as due to the breakdown of the inversion symmetry in a given experiment. Yet in a number of theoretical calculations, the emergence of even harmonics has to rely on more complicated theoretical models. In particular, in[20] it was stated that ' *a two-band model with one conduction and one valence band cannot explain the occurrence of even harmonics in the emission spectrum. For this reason, we generalize the theory presented in Refs. 9 and 10 beyond a 2-band description.*". In [28], it stated that *"it is not possible to account for even harmonics generated directly from crystalline ZnO only with a two-band model"*. Alternatively, a second harmonic of the driving field was added artificially to account for the appearance of even harmonics [9]. Thus, in the first two references the origin of even harmonics was attributed to the lack of convergence of a two-band model and a multi-band model is required. Intuitively this is inconsistent

since a multi-band calculation may improve the accuracy of the calculation but not the appearance of "new" spectral features. In the third reference, the appearance of even harmonics was attributed to the asymmetry of the laser light. If this is true, then even harmonics should be observed in solids in all systems.

In the present work, we offer a much simpler interpretation of the appearance of even harmonics in solids that is consistent with the intuitive picture that even harmonics occur due to the breakdown of inversion symmetry in the solids. A simple two-band model is able to predict the generation of even harmonics for such systems. We traced the failure of the earlier works to the approximations made on the dipole transition elements where the transition dipole phase (TDP) was neglected. In this approximation, the broken symmetry of the system was inadvertently "restored", thus resulting in the disappearance of even harmonics. Thus, in this article, we investigated the role of TDP in the generation of harmonics in solids. We emphasize the importance of treating the TDP correctly in the theory for a correct interpretation of experimental HHG data. TDP has not been widely investigated in linear optical physics. In the nonlinear HHG in solids, the broadband nature of the interaction requires the correct treatment of TDP over a broad spectral region. Such a requirement poses additional challenge in the HHG theory in solids since most commercial software packages do not treat the TDP correctly. Thus in the present work, we took to study HHG in graphene where the band structure can be approximately calculated using the tight-binding model. We used the two-band model to illustrate how even harmonics are generated for systems that exhibit broken symmetry.

In Section II we begin with a brief account of the theory. The role of TDP is demonstrated in Sec. III by calculations of HHG spectra from graphene (with inversion symmetry) and gapped graphene (without inversion symmetry). In graphene the TDP can be ignored and only odd harmonics exist, while in gapped graphene the TDP cannot be neglected and both even and odd harmonics are generated. In Sec. IV we studied the role of TDP in the generation of even harmonics from the quantum orbits point of view. In Sec. V we investigate whether the structure of a crystal in a dynamic system can be revealed by monitoring the strength of even harmonics by deforming the lattice geometry of a crystal. Based on this study, we found that the lattice separation has to be substantially reduced before the even harmonics can become comparable to the odd harmonics in strength. On the other hand, strength of even harmonics grows rapidly when the lattice distance is reduced even if just by a few percent. Future experimental studies should investigate whether even harmonics in a solid can be used to probe the change of lattice separations in a dynamic system. We summarize this article in Sec. VI. Atomic units are used throughout this article unless otherwise noted.

II. BASIC THEORY

A. The semiconductor Bloch equations

The SBEs, which were derived from TDSE in the length gauge under the single-electron approximation, are used in this work to calculate the HHG spectra from crystals. Consider two energy bands in the HHG process. As in semiconductors, the upper band is treated as the conduction band ("c") while the lower band is the valence band ("v"). For a two-band model, the SBEs read:

$$\frac{\partial p_{cv}(\mathbf{k},t)}{\partial t} = \left(-iE_g(\mathbf{k}) - \frac{1}{T_2}\right)p_{cv}(\mathbf{k},t)$$
$$+\mathbf{F}(t)\cdot\nabla_{\mathbf{k}}p_{cv}(\mathbf{k},t)$$
$$+i\left[\rho_c(\mathbf{k},t) - \rho_v(\mathbf{k},t)\right]\mathbf{F}(t)\cdot\mathbf{D}_{cv}(\mathbf{k}), \quad (1)$$

$$\frac{\partial \rho_v(\mathbf{k},t)}{\partial t} = -2\mathrm{Im}\left\{\mathbf{F}(t)\cdot\mathbf{D}_{cv}(\mathbf{k})p_{cv}(\mathbf{k},t)\right\}$$
$$+\mathbf{F}(t)\cdot\nabla_{\mathbf{k}}\rho_v(\mathbf{k},t), \quad (2)$$

$$\frac{\partial \rho_c(\mathbf{k},t)}{\partial t} = 2\mathrm{Im}\left\{\mathbf{F}(t)\cdot\mathbf{D}_{cv}(\mathbf{k})p_{cv}(\mathbf{k},t)\right\}$$
$$+\mathbf{F}(t)\cdot\nabla_{\mathbf{k}}\rho_c(\mathbf{k},t). \quad (3)$$

Here $p_{cv}(\mathbf{k},t)$ is the micropolarization between the conduction band and the valence band. $E_g(\mathbf{k}) = E_c(\mathbf{k}) - E_v(\mathbf{k})$ is the energy difference between the two bands, $\rho_{c(v)}(\mathbf{k},t)$ is the electron density in the conduction (valence) band. T_2 is the interband dephasing time. In this paper, T_2 is set to 1 fs for graphene as used in [3, 22, 27]. $\mathbf{F}(t) = \hat{\varepsilon}F(t)$ is the electric field of the laser pulse with $\hat{\varepsilon}$ being the polarization direction. $\mathbf{D}_{cv}(\mathbf{k})$ is the transion dipole moment (TDM) between the valence band and the conduction band which can be calculated by

$$\mathbf{D}_{cv}(\mathbf{k}) = i\int_{cell} u^*_{c,\mathbf{k}}(\mathbf{r})\nabla_{\mathbf{k}}u_{v,\mathbf{k}}(\mathbf{r})d\mathbf{r}, \quad (4)$$

where $u_{c(v),\mathbf{k}}(\mathbf{r})$ is the periodic part of the Bloch wave function for the conduction (valence) band with crystal momentum $\mathbf{k}$. The derivation of the SBEs starting from the TDSE is given in Appendix A. The SBEs are solved by finite difference method with constant time grid $\Delta t = 0.00025$ a.u. and crystal momentum grid $\Delta k = 0.00001$ a.u..

After solving the SBEs, one can obtain the intraband current

$$\mathbf{J}_{\mathrm{intra}}(t) = \sum_{\lambda=c,v}\int_{BZ}\mathbf{v}_\lambda(\mathbf{k})\rho_\lambda(\mathbf{k},t)d\mathbf{k}, \quad (5)$$

and the interband current

$$\mathbf{J}_{\mathrm{inter}}(t) = \frac{\partial}{\partial t}\int_{BZ}\mathbf{D}_{cv}(\mathbf{k})p_{cv}(\mathbf{k},t)d\mathbf{k} + c.c., \quad (6)$$

where $\mathbf{v}_\lambda(\mathbf{k}) = \nabla_\mathbf{k} E_\lambda(\mathbf{k})$ is the group velocity. In this work we are interested in the spectrum of parallel harmonics, which is proportional to the absolute square of the projection of the Fourier-transformed total current onto the polarization direction $\hat{\varepsilon}$, i.e.

$$S_{\mathrm{HHG}}(\omega) \propto \left| \hat{\varepsilon} \cdot \int_{-\infty}^{\infty} \left[\mathbf{J}_{\mathrm{intra}}(t) + \mathbf{J}_{\mathrm{inter}}(t) \right] e^{i\omega t} dt \right|^2 . \quad (7)$$

B. Properties of TDM with respect to crystal symmetry

The TDM, the $\mathbf{D}_{cv}(\mathbf{k})$ given in Eq. (4) is an important quantity in HHG processes. Here we discuss what properties should the TDM have if the crystal has certain spatial symmetry. To begin with, the wave function $u_{m,\mathbf{k}}(\mathbf{r})$ satisfies the $\mathbf{k} \cdot \mathbf{p}$ eigenvalue equation:

$$\left(-\frac{1}{2}\nabla_\mathbf{r}^2 + V(\mathbf{r}) - i\mathbf{k} \cdot \nabla_\mathbf{r} \right) u_{m,\mathbf{k}}(\mathbf{r})$$
$$= \left(E_m(\mathbf{k}) - \frac{k^2}{2} \right) u_{m,\mathbf{k}}(\mathbf{r}), \quad (8)$$

where $E_m(\mathbf{k})$ is the energy eigenvalue for band m with a crystal momentum $\mathbf{k}$, and $V(\mathbf{r})$ is the periodic potential of the crystal used in the one-electron model.

In Eq. (8) if we replace $\mathbf{k}$ by $-\mathbf{k}$, noting that $E_m(-\mathbf{k}) = E_m(\mathbf{k})$, then

$$\left(-\frac{1}{2}\nabla_\mathbf{r}^2 + V(\mathbf{r}) + i\mathbf{k} \cdot \nabla_\mathbf{r} \right) u_{m,-\mathbf{k}}(\mathbf{r})$$
$$= \left(E_m(\mathbf{k}) - \frac{k^2}{2} \right) u_{m,-\mathbf{k}}(\mathbf{r}). \quad (9)$$

On the other hand, if we take the complex conjugate of Eq. (8), then

$$\left(-\frac{1}{2}\nabla_\mathbf{r}^2 + V(\mathbf{r}) + i\mathbf{k} \cdot \nabla_\mathbf{r} \right) u_{m,\mathbf{k}}^*(\mathbf{r})$$
$$= \left(E_m(\mathbf{k}) - \frac{k^2}{2} \right) u_{m,\mathbf{k}}^*(\mathbf{r}). \quad (10)$$

Consider non-degenerate energy bands, from Eqs. (9) and (10) we can set $u_{m,-\mathbf{k}}(\mathbf{r}) = u_{m,\mathbf{k}}^*(\mathbf{r})$. Then from Eq. (4) one obtains a general property

$$\mathbf{D}_{cv}(-\mathbf{k}) = \mathbf{D}_{cv}^*(\mathbf{k}) \quad (11)$$

for any crystal. If the crystal has inversion symmetry, $V(\mathbf{r}) = V(-\mathbf{r})$, by replacing $\mathbf{r}$ by $-\mathbf{r}$ in Eq. (8), we have

$$\left(-\frac{1}{2}\nabla_\mathbf{r}^2 + V(\mathbf{r}) + i\mathbf{k} \cdot \nabla_\mathbf{r} \right) u_{m,\mathbf{k}}(-\mathbf{r})$$
$$= \left(E_m(\mathbf{k}) - \frac{k^2}{2} \right) u_{m,\mathbf{k}}(-\mathbf{r}). \quad (12)$$

Comparing Eq. (12) to (9) we find $u_{m,\mathbf{k}}(-\mathbf{r}) = \pm u_{m,-\mathbf{k}}(\mathbf{r})$; then from Eq. (4),

$$\mathbf{D}_{cv}(-\mathbf{k}) = \pm\mathbf{D}_{cv}(\mathbf{k}). \quad (13)$$

Therefore for crystals with inversion symmetry, the TDM $\mathbf{D}_{cv}(\mathbf{k})$ is either even or odd with respect to $\mathbf{k}$.

Moreover, consider if the crystal has no inversion symmetry but has reflection symmetry with respect to a symmetry plane. Let $\mathbf{n}$ be the unit vector perpendicular to the symmetry plane (normal direction), we can introduce a reflection operation $T_\mathbf{n}\mathbf{r} = \mathbf{r} - 2(\mathbf{r} \cdot \mathbf{n})\mathbf{n}$ such that $V(T_\mathbf{n}\mathbf{r}) = V(\mathbf{r})$. From Eq. (8),

$$\left(-\frac{1}{2}\nabla_{T_\mathbf{n}\mathbf{r}}^2 + V(T_\mathbf{n}\mathbf{r}) - i\mathbf{k} \cdot \nabla_{T_\mathbf{n}\mathbf{r}} \right) u_{m,\mathbf{k}}(T_\mathbf{n}\mathbf{r})$$
$$= \left(-\frac{1}{2}\nabla_\mathbf{r}^2 + V(\mathbf{r}) - i\left(T_\mathbf{n}\mathbf{k} \right) \cdot \nabla_\mathbf{r} \right) u_{m,\mathbf{k}}(T_\mathbf{n}\mathbf{r})$$
$$= \left(E_m(\mathbf{k}) - \frac{k^2}{2} \right) u_{m,\mathbf{k}}(T_\mathbf{n}\mathbf{r}). \quad (14)$$

Since $E_m(T_\mathbf{n}\mathbf{k}) = E_m(\mathbf{k})$, we can find $u_{m,\mathbf{k}}(T_\mathbf{n}\mathbf{r}) = \pm u_{m,T_\mathbf{n}\mathbf{k}}(\mathbf{r})$. Finally from Eq. (4) we can obtain a relation for the TDM when the crystal has reflection symmetry:

$$\hat{\eta} \cdot \mathbf{D}_{cv}(T_\mathbf{n}\mathbf{k}) = \pm T_\mathbf{n}(\hat{\eta}) \cdot \mathbf{D}_{cv}(\mathbf{k}), \quad (15)$$

where $\hat{\eta}$ can be any unit vector. A particular case of interest is when $\hat{\eta} = \mathbf{n}$ and $\mathbf{k} = k\mathbf{n}$, in which

$$\mathbf{n} \cdot \mathbf{D}_{cv}(-k\mathbf{n}) = \mp\mathbf{n} \cdot \mathbf{D}_{cv}(k\mathbf{n}). \quad (16)$$

For the HHG processes considered in this work, the TDM that contributes most to the parallel harmonic can be reduced to a scalar function $D_{\parallel,cv}(k) = \hat{\varepsilon} \cdot \mathbf{D}_{cv}(\hat{\varepsilon}k)$. Here $\hat{\varepsilon}$ is the laser polarization direction, and the crystal momentum $\mathbf{k}$ is confined along this direction.

For the system that has inversion symmetry, Eqs. (11) and (13) imply

$$D_{\parallel,cv}(-k) = D_{\parallel,cv}^*(k), \quad (17)$$

and

$$D_{\parallel,cv}(-k) = \pm D_{\parallel,cv}(k). \quad (18)$$

Therefore the TDM $D_{\parallel,cv}(k)$ can only take two forms: a real and even function, or a pure imaginary and odd function of k. In either case its phase is trivial and not important.

On the other hand, only Eq. (17) holds if there is no symmetry, The TDM can then be expressed as

$$D_{\parallel,cv}(k) = |D_{\parallel,cv}(k)|e^{i\theta(k)}. \quad (19)$$

Here $\theta(k)$ is the non-trivial TDP which is an odd function of k.

For the crystal that has reflection symmetry, the property of TDM depends on the polarization direction. If $\hat{\varepsilon} \parallel \mathbf{n}$, then from Eq. (16) we can see Eq. (18) still hold for $D_{\parallel,cv}(k)$, just as in the case with inversion symmetry. However, if the polarization direction $\hat{\varepsilon}$ is not parallel to the normal direction of the symmetry plane, Eq. (18) is not valid, and the TDP, $\theta(k)$, as given in Eq. (19),

cannot be ignored. In other words, ignoring the TDP is equivalent to introducing additional symmetry that is not present in the problem, thus resulting in the disappearance of even harmonics.

In previous papers, the TDMs were calculated approximately by first-order $\mathbf{k} \cdot \mathbf{p}$ theory where the $\theta(k)$ was not taken into account. Strictly speaking, the first-order $\mathbf{k} \cdot \mathbf{p}$ approximation is valid only when $\mathbf{k}$ is close to Γ or other high-symmetry points. When interacting with strong laser fields, the electrons would be driven away from the high-symmetry points and even travel through the entire Brillouin zone, thus the first-order $\mathbf{k}\cdot\mathbf{p}$ approximation is not appropriate. In our previous papers[21, 24] and reference [29], the absolute values of the k-dependent TDMs are calculated from the density functional theory (DFT). However, based on the above analysis, ignoring the TDP is not justified for a system without symmetry.

To conclude this section, the TDP will reflect the spatial symmetry of the solid. For a crystal without inversion symmetry, the TDP should be taken into account. In the following sections we will take the graphene (with inversion symmetry) and the gapped graphene (without inversion symmetry) as examples to demonstrate the role of TDP in the HHG process.

III. HARMONICS FROM GRAPHENE AND GAPPED GRAPHENE

The interaction of a strong laser field with graphene, or graphene-like materials, has been studied theoretically [30–33] and in a recent experiment [34]. Here, we choose model graphene and gapped graphene for several reasons. First, relatively pure graphene can be grown in the laboratory. Second, gapped graphene with broken symmetry can be grown on substrates. Third, as a two-dimensional material, graphene or gapped graphene can be easily treated by the tight-binding approximation[35]where analytical expressions for the energy bands and the TDM can be derived. Since it is not trivial to obtain accurate TDP from DFT-based commercial softwares, the TDM obtained from analytical expressions is particularly important.

The lattice structure and the 2D first Brillouin zone of graphene or gapped graphene are shown in Figs. 1(a) and (b), respectively. There are two atoms per unit cell, labeled by "A" and "B" in Fig. 1(a). When both of these two sites are occupied by carbon, the system is graphene with inversion symmetry. If the graphene is grown on SiC substrate these two sites become inequivalent and the system becomes a gapped graphene that has no inversion symmetry. Assuming that only the $2p_z$ wavefunction of each atom contributes to the Bloch wavefunction, based on the nearest-neighbor interactions and tight-binding approximation, analytical expressions of the energy band and the wavefunction for graphene-like materials can be derived:

$$E_{c/v}(\mathbf{k}) = \pm \sqrt{\frac{\Delta^2}{4} + |g(\mathbf{k})|^2}, \qquad (20)$$

$$|n,\mathbf{k}\rangle = \frac{1}{\sqrt{2}} \begin{pmatrix} e^{i\alpha(\mathbf{k})/2}\sqrt{\left(E_n(\mathbf{k}) + \frac{\Delta}{2}\right)/E_n(\mathbf{k})} \\ \pm e^{-i\alpha(\mathbf{k})/2}\sqrt{\left(E_n(\mathbf{k}) - \frac{\Delta}{2}\right)/E_n(\mathbf{k})} \end{pmatrix}, \qquad (21)$$

where

$$g(\mathbf{k}) = \gamma_1 e^{i\mathbf{k}\cdot\mathbf{R}_1} + \gamma_2 e^{i\mathbf{k}\cdot\mathbf{R}_2} + \gamma_3 e^{i\mathbf{k}\cdot\mathbf{R}_3}. \qquad (22)$$

In the above equations, $|n,\mathbf{k}\rangle$ denotes the Bloch wave function of the conduction band ("c") or the valence band ("v"). The positive sign in "$\pm$" is for the conduction band while the negative sign is for the valence band. Δ is the energy gap at K points, $\Delta = 0$ for graphene with inversion symmetry, while $\Delta > 0$ for gapped graphene without inversion symmetry. $\gamma_1, \gamma_2, \gamma_3$ are the two-center hopping integrals which depend on bond length[36]. The vectors $\mathbf{R}_1, \mathbf{R}_2, \mathbf{R}_3$ are shown in Fig. 1(a) which describe the spatial structure of the system. The factor $\alpha(\mathbf{k}) = \arg\{f(\mathbf{k})\}$ with

$$f(\mathbf{k}) = e^{i\mathbf{k}\cdot\mathbf{R}_1} + e^{i\mathbf{k}\cdot\mathbf{R}_2} + e^{i\mathbf{k}\cdot\mathbf{R}_3}. \qquad (23)$$

In this work we choose $\gamma_1 = \gamma_2 = \gamma_3 = -3.03$ eV, $|\mathbf{R}_1| = |\mathbf{R}_2| = |\mathbf{R}_3| = 1.42$ Å, and $\Delta = 1$ eV for the gapped graphene.

By inserting the Bloch wave functions into Eq. (4), an analytical expression for the TDM is obtained:

$$\mathbf{D}_{cv}(\mathbf{k}) = -\frac{|g(\mathbf{k})|}{2E_c(\mathbf{k})}\nabla_\mathbf{k}\alpha(\mathbf{k}) + i\frac{\Delta}{4E_c^2(\mathbf{k})}\nabla_\mathbf{k}|g(\mathbf{k})|. \quad (24)$$

More explicitly, the TDM for the graphene is

$$D_{x,cv}(\mathbf{k}) = \frac{a}{2\sqrt{3}}\frac{1 + \cos(\frac{ak_y}{2})\left[\cos(\frac{3ak_x}{2\sqrt{3}}) - 2\cos(\frac{ak_y}{2})\right]}{1 + 4\cos(\frac{ak_y}{2})\left[\cos(\frac{3ak_x}{2\sqrt{3}}) + \cos(\frac{ak_y}{2})\right]}, \qquad (25)$$

$$D_{y,cv}(\mathbf{k}) = \frac{a}{2}\frac{\sin(\frac{ak_y}{2})\sin(\frac{\sqrt{3}ak_x}{2})}{1 + 4\cos(\frac{ak_y}{2})\left[\cos(\frac{3ak_x}{2\sqrt{3}}) + \cos(\frac{ak_y}{2})\right]}, \qquad (26)$$

and for the gapped graphene is

$$D_{x,cv}(\mathbf{k}) = \frac{a\gamma\left[\cos(\frac{3ak_x}{2\sqrt{3}})\cos(\frac{ak_y}{2}) - \cos(ak_y)\right]}{2\sqrt{3}E_c(\mathbf{k})|f(\mathbf{k})|} \\ + i\frac{a\Delta\gamma\left[\sqrt{3}\sin(\frac{3ak_x}{2\sqrt{3}})\cos(\frac{ak_y}{2})\right]}{4E_c^2(\mathbf{k})|f(\mathbf{k})|}, \qquad (27)$$

$$D_{y,cv}(\mathbf{k}) = \frac{a\gamma}{2E_c(\mathbf{k})|f(\mathbf{k})|}\sin(\frac{\sqrt{3}ak_x}{2})\sin(\frac{ak_y}{2}) \\ + i\frac{a\Delta\gamma\left[\cos(\frac{\sqrt{3}ak_y}{2})\sin(\frac{ak_y}{2}) + \sin(ak_y)\right]}{4E_c^2(\mathbf{k})|f(\mathbf{k})|}, \qquad (28)$$

where $a = |\mathbf{a}_1| = |\mathbf{a}_2| = 2.46$ Å, see Fig. 1(a).

As expected, for the graphene with inversion symmetry, the $\mathbf{D}_{cv}(\mathbf{k})$ is a real and even function with respect to $\mathbf{k}$, and the TDP is zero. On the other hand, the expression of the transition dipole for the gapped graphene is a complex quantity and it only satisfies Eq. (11) in general. We take the $\Gamma-$M direction as the x axis, the y axis is taken along the $\Gamma-$K direction, as shown in Fig. 1.

If the laser is polarized along the x direction, the energy bands of graphene and gapped graphene are shown along the Γ-M direction is shown in Fig. 1(c). Note that Γ point is always the $\mathbf{k} = (\mathbf{0}, \mathbf{0})$ point, but in all of the figures in this paper we put the +M (-M) point at the center where the minimum band gap is located. The energy bands between the two materials are nearly the same. Along the Γ-M direction, the amplitude and phase of the dipole transition moment are shown in Figs. 1(e) and (d), respectively. The magnitude of the dipole moment for the two materials are also very closed to each other. On the other hand, there is a clear difference in the TDP. The TDP for graphene is zero, but for gapped graphene there is a small but non-negligible value. This nonzero TDP will be responsible for the generation of even harmonics. Also note that the energy gap, shown in Fig. 1(c), is smallest near the M point, and the transition dipole amplitude is also narrowly peaked at the M point, thus the harmonics are expected to be dominated by this portion of the Brillouin zone. The TDP is taken from Eq. (27) for polarization along the x direction.

If the laser is polarized along the y direction, $D_{\parallel,cv}(k) = D_{y,cv}(k\hat{y})$, Eq. (28) implies that the TDM for gapped graphene becomes an odd and pure imaginary function of k which is a trivial constant phase that can be ignored. This is not surprising because the gapped graphene has reflection symmetry with respect to the $x - z$ plane, with $\hat{y}$ being its normal direction. The energy band along the $\Gamma-$K direction, with $(+/-)$ K at the center, has a similar shape as in Figs. 1(c) except that the energy gap is only about 1 eV. While the constant phase of $D_{y,cv}(k\hat{y})$ can be ignored, the magnitude of this dipole diverges at the $(+/-)$ K point. This can be seen by rewriting $f(\mathbf{k})$ as

$$f(\mathbf{k}) = e^{i\frac{ak_x}{\sqrt{3}}} + 2e^{-i\frac{ak_x}{2\sqrt{3}}}\cos(\frac{ak_y}{2}) \qquad (29)$$

by setting each $|\mathbf{R}_i|$ to $a/\sqrt{3}$ in Eq.(23). Along the y-axis where $ak_x=0$, $f(\mathbf{k})$ goes to zero when $ak_y = 4\pi/3$, which corresponds to the $(+/-)$ K point. The existence of such a singular point in the transition dipole will make the HHG calculation along the y axis less accurate.

High-order harmonic spectra from graphene and gapped graphene are calculated by SBEs and presented in Fig. 2. Here the laser parameters are 10 fs in FWHM duration, 800 nm in wavelength and 2×10^{12} W/cm^2 in peak intensity. For the graphene, only odd harmonics are observed. For the gapped graphene, with laser polarized along the y direction, only odd harmonics appear. In
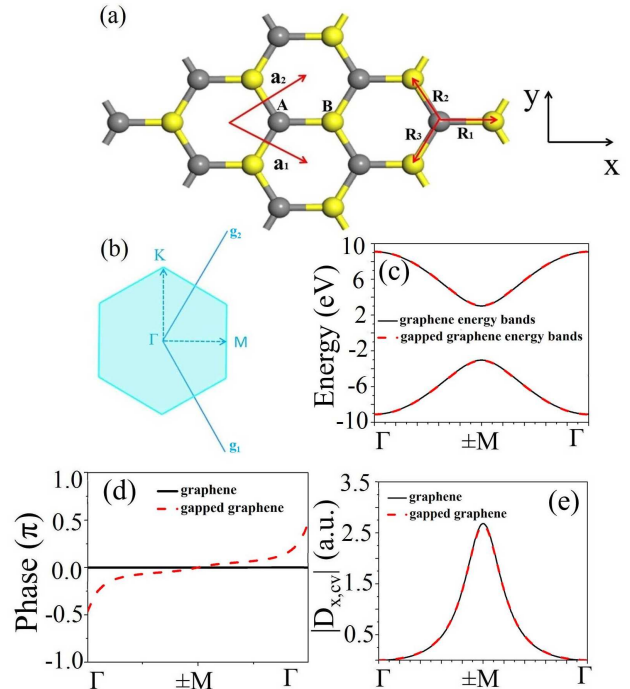

FIG. 1. (a) Hexagonal lattice structure of 2D graphene or gapped graphene. $\mathbf{a_i}$ is the unit vector in real space. The unit cell contains two atoms labeled by "A" and "B". If both of these two sites are occupied with carbon, the system is graphene. If these two sites are inequivalent, the system becomes gapped graphene. The x and y axes are also indicated. (b) The first Brillouin zone of graphene or gapped graphene. $\mathbf{g_i}$ is the reciprocal lattice vector. High symmetry points, Γ, M and K, are labeled. (c) Energy bands of graphene (black solid lines) and gapped graphene (red dashed lines) along the direction of Γ-M. The band structures for graphene and gapped graphene are nearly the same. Note that the band structure was presented using the M point at the center. (d) Transition dipole phases (TDP) of graphene (black solid line) and gapped graphene (red dashed line) in the direction of Γ-M. The TDP of graphene is zero for all crystal momentum due to the inversion symmetry. In contrast, there exists a non-zero TDP for gapped graphene along the x-axis. (e) Absolute values of transition dipole moments along Γ-M direction for graphene (black solid line) and gapped graphene (red dashed line). The behavior of band structure and transition dipole along the y-axis is explained in the text.

contrast, even harmonics come into appearance when the laser is polarized along the x direction as the symmetry is broken. The even harmonics are closely related to the TDP that reflects the symmetry of the system. This has been confirmed by our numerical calculation. Once we remove the phase of the transition dipole in the gapped graphene, the even harmonics disappear in the calculated HHG spectra.

In Fig. 2 the harmonic yields for the gapped graphene in the y direction is much larger than in the x direction.
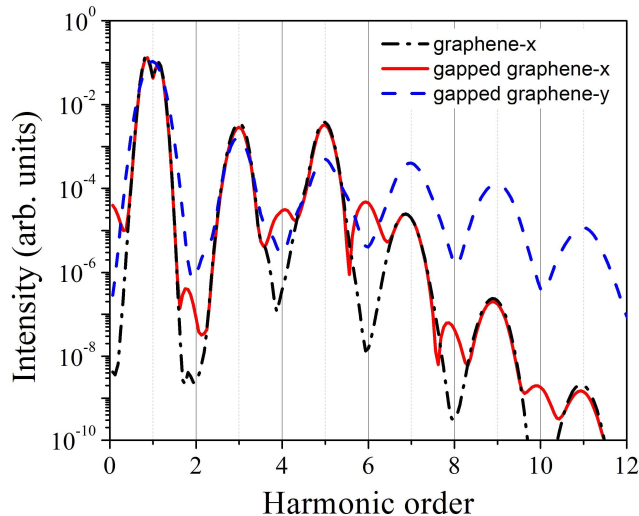
FIG. 2. Calculated HHG spectra for graphene with laser polarized along the x direction (black dash-dotted line), gapped graphene with laser polarized along the x direction (red solid line), and gapped graphene with laser polarized along the y direction (dashed blue line). Laser parameters are 10 fs in FWHM duration, 800 nm in wavelength and 2×10^{12} W/cm^2 in peak intensity.

FIG. 3. Dependence of the efficiency of the 2nd to 5th harmonic from gapped graphene on laser parameters. The laser is polarized along the x direction (without symmetry). In (a) and (b), the laser wavelength is fixed to be 800 nm while the intensity is tuned from 1×10^{12} to 3×10^{13} W/cm^2. In (c) and (d), the laser intensity is fixed to be 2×10^{12} W/cm^2 while the wavelength is tuned from 800 nm to 2000 nm.

A normalization factor of 200 was used to match the intensity of the first harmonic. The resulting curve for the y harmonics become dropping down much slower than the x harmonics. However, as pointed out earlier, the dipole amplitude along the y axis has singularity at the $+/-$ K points. The numerical calculations under this circumstance may be less accurate. This is a topic that will require further investigation in the future.

From Fig. 2 it is obvious that the intensity of even harmonics is much lower than the odd harmonics. We explore what factors influence the strength of even harmonics. Define a parameter P_i for the efficiency of the generation of different harmonics from the 2nd to the 5th order, we show its dependence on laser intensity and wavelength in Fig. 3. We note that even harmonics are always lower by three orders between the 2nd and 3rd harmonics, and by one order between 4th and 5th harmonics. It appears that for the 2nd and 3rd harmonics their ratios are nearly independent of the intensity and the wavelength. For the 4nd and 5rd harmonics, the dependence on the laser intensity is less smooth. The wavelength dependence does appear to have a minimum near 1300 nm. Such dependence presented here is to serve a first order estimate only since it is expected that at higher laser intensities multiband model will be needed. Further extension of the present model to multiband calculations will be needed to draw more accurate conclusions.
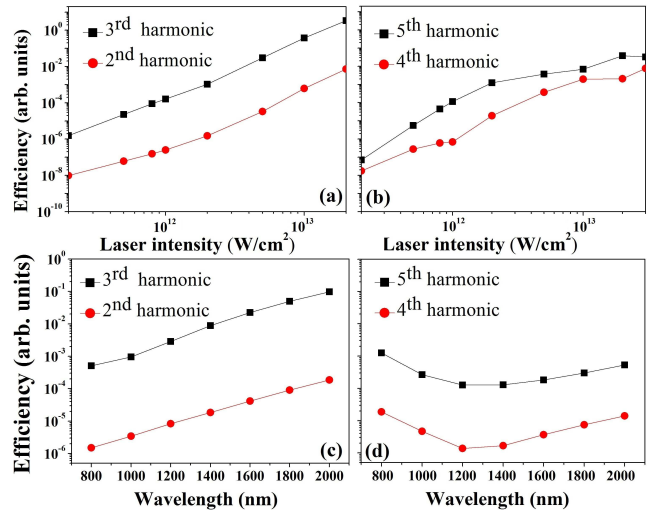
IV. RELATIONSHIP BETWEEN THE EFFICIENCY OF EVEN HARMONICS AND THE TDP

In order to find out why even harmonics are much weaker than odd harmonics, it is instructive to simplify the SBEs model and follow the Keldysh's approach as presented in Ref. [37]. In general, both intraband and interband transitions will contribute to the harmonic generation from solids. In Keldysh's approach these two components are treated separately. Assuming $\rho_v(\mathbf{k}, t) - \rho_c(\mathbf{k}, t) = 1$, i.e., excitation to the conduction band is small, then the interband and intraband components can be calculated respectively by:

$$J_{\parallel,\text{inter}}(\omega) = -i\omega \int_{BZ} d\mathbf{k}\hat{\varepsilon} \cdot \mathbf{D}^*_{cv}(\mathbf{k}) \int_{-\infty}^{\infty} dt e^{-i\omega t} \int_{-\infty}^{t} dt'$$

$$\times F(t')\hat{\varepsilon} \cdot \mathbf{D}_{cv}[\mathbf{k} + \mathbf{A}(t) - \mathbf{A}(t')]e^{-iS(\mathbf{k},t,t')}e^{-\frac{t-t'}{T_2}} + c.c.$$

$$(30)$$

$$J_{\parallel,\text{intra}}(\omega) = \sum_{\lambda=c,v} \int_{BZ} \mathbf{v}_\lambda(\mathbf{k})\hat{\varepsilon} \int_{-\infty}^{\infty} dt\, e^{-i\omega t}$$

$$\times \int_{-\infty}^{t} dt'\, F(t')\hat{\varepsilon} \cdot \mathbf{D}_{cv}^*[\mathbf{k} + \mathbf{A}(t) - \mathbf{A}(t')]$$

$$\times \int_{-\infty}^{t'} dt''\, F(t'')\hat{\varepsilon} \cdot \mathbf{D}_{cv}[\mathbf{k} + \mathbf{A}(t) - \mathbf{A}(t'')]$$

$$\times e^{-iS(\mathbf{k},t',t'')} e^{-\frac{t'-t''}{T_2}} + c.c.$$

$$(31)$$

where ω is the frequency of the generated harmonic, $S(\mathbf{k},t,t') = \int_{t'}^{t} E_g(\mathbf{k}_\tau)d\tau$ with $\mathbf{k}_\tau = \mathbf{k} + \mathbf{A}(t) - \mathbf{A}(\tau)$ is the action, and $\mathbf{A}(t) = -\hat{\varepsilon} \int_{-\infty}^{t} F(t')dt'$ is the vector potential of the laser field.

First, we focus on the interband component. Based on saddle point analysis in Ref. [37], we can write $J_{\parallel,\text{inter}}(\omega)$ as a coherent sum of contributions from a set of quantum orbits that are labeled by $(\mathbf{k}_s, t_s, t'_s)$. To simplify the discussion, consider the saddle point solution of the crystal momentum $\mathbf{k}_s$ to be along the $\hat{\varepsilon}$ direction, then all the vectors are reduced to scalars. The interband current due to a single quantum orbit is proportional to

$$D_{\parallel,cv}^*(k_s)D_{\parallel,cv}(k'_s)F(t'_s)e^{-i\omega t_s - iS(k_s,t_s,t'_s) - \frac{t_s-t'_s}{T_2}}. \quad (32)$$

with $D_{\parallel,cv}(k) = \hat{\varepsilon} \cdot \mathbf{D}_{cv}(k\hat{\varepsilon})$, as given before. The quantum orbit can be interpreted as follows: the electron is excited from the valence band to the conduction band at time t'_s with crystal momentum $k'_s = k_s + A(t_s) - A(t'_s)$, then it is driven by the laser field in the conduction band and acquiring a phase $e^{-iS(k_s,t_s,t'_s)}$. Finally it recombines back to the valence band at time t_s with crystal momentum k_s, accompanied by the emission of a photon. More detail about the semiclassical analysis can be found in Ref. [38, 39].

For a multi-cycle electric field $F(t)$ with an optical period T, due to the periodicity of the electric field, the quantum orbit corresponding to $(-k_s, t_s + T/2, t'_s + T/2)$ results in the same harmonic energy as the quantum orbit corresponding to (k_s, t_s, t'_s). Using $F(t + T/2) = -F(t)$, the coherent sum of the interband current resulting from such a pair of orbits that are separated by one-half optical period is proportional to

$$\left[D_{\parallel,cv}^*(k_s)D_{\parallel,cv}(k'_s) - D_{\parallel,cv}^*(-k_s)D_{\parallel,cv}(-k'_s)e^{-i\omega\frac{T}{2}} \right]$$

$$\times F(t'_s)e^{-i\omega t_s}e^{-iS(k_s,t_s,t'_s)}e^{-\frac{t_s-t'_s}{T_2}}. \quad (33)$$

Therefore the yield of the N_{th} harmonic is proportional to $|\Delta_N|^2$ where the factor Δ_N is given by

$$\Delta_N = D_{\parallel,cv}^*(k_s)D_{\parallel,cv}(k'_s) - D_{\parallel,cv}^*(-k_s)D_{\parallel,cv}(-k'_s)e^{-iN\pi}. \quad (34)$$

If the system has symmetry such that Eq. (18) holds, then $\Delta_N = D_{\parallel,cv}^*(k_s)D_{\parallel,cv}(k'_s)(1 - e^{-iN\pi})$. Clearly

$\Delta_N = 0$ for even harmonics, therefore the harmonic spectrum consists of odd harmonics only. This situation is similar to HHG in atoms. On the other hand, with broken symmetry we only have Eqs. (17) and (19), then

$$\Delta_N = |D_{\parallel,cv}(k_s)| \, |D_{\parallel,cv}(k'_s)|$$

$$\times \left\{ e^{i[\theta(k'_s) - \theta(k_s)]} - e^{-i[\theta(k'_s) - \theta(k_s)]}e^{-iN\pi} \right\}. \quad (35)$$

One can deduce that for odd harmonics $|\Delta_N|^2 \propto \cos^2[\theta(k'_s) - \theta(k_s)]$, and for even harmonics $|\Delta_N|^2 \propto \sin^2[\theta(k'_s) - \theta(k_s)]$. Because the laser field is strong, in the reciprocal space the recombination could occur with a crystal momentum far from where the electron was excited into the conduction band. Thus in general there will be even harmonics if the crystal does not have inversion symmetry or does not have reflection symmetry with respect to the plane perpendicular to the laser polarization direction. The strength of even harmonics depends on the difference in the transition dipole phase at the subcycle ionization time and return time: $\Delta\theta = |\theta(k'_s) - \theta(k_s)|$. The even harmonics are much weaker than the the odd harmonics when $\Delta\theta$ is close to $n\pi$, and the opposite happens when $\Delta\theta$ is close to $\pi/2 + n\pi$.

Similar analysis for intraband transition is more difficult since Eq. (31) is a four dimensional integral. There is no analytical expression like Eq. (35) available for intraband transitions. Qualitatively, however, one can still draw the same conclusion that efficient generation of even harmonics relies on the TDP, see Appendix B.

In Fig. 4, we present the time-frequency analysis of the harmonic spectrum for gapped graphene in (a), the electric field and vector potential in (b), the time-dependent electron density in the conduction band in (c), as well as the k-dependent TDP in (d). From Fig. 4 we can see that electrons are excited mostly at time t' when $A(t') = 0$. Then the electrons are driven by the electric field in the conduction band. During the motion in the conduction band, there are some probabilities to make the transition from the conduction band to the valence band accompanied by the emission of a photon. The labels K_1 and K_2 indicate a pair of electron orbits that are separated by one-half optical period. As discussed above, these two quantum orbits will add coherently. The strength of even harmonics is limited by the difference in TDP ($\Delta\theta$) that a quantum orbit can accumulate. For gapped graphene, as shown in Fig. 4(d), the k-dependent TDP is very flat such that $\Delta\theta$ does not exceed 0.07π. This explains why the efficiency of even harmonics is much lower than the odd harmonics as shown in Fig. 3.

V. STUDY OF EVEN HARMONICS VERSUS LATTICE DISPLACEMENT

In the previous sections the even harmonics for the gapped graphene, due to its small TDP, are relatively weak. From Eqs. (20) to (22), the TDP can be seen to
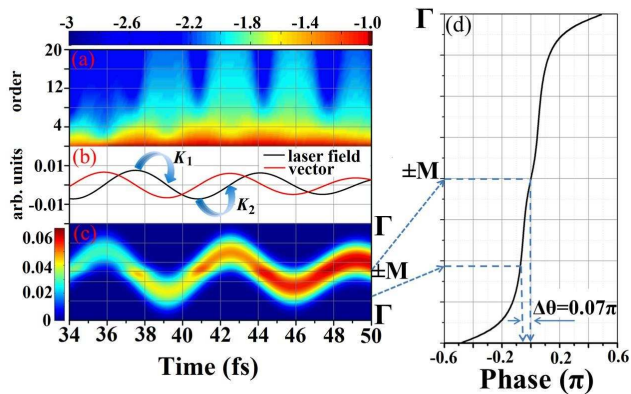
8

FIG. 4. (a) Time-frequency analysis of HHG from gapped graphene with laser polarized along the x direction. The HHG intensities are depicted on logarithmic scale. (b) The black solid line is the electric field, and the red solid line is the vector potential of the laser field, each is relatively normalized. The two arrows indicate two symmetric electron orbits K_1 and K_2, see Eq. (30). Electrons are excited into the conduction band at the starting point of the arrow, and recombine to the valence band at the ending point of the arrow with a photon emitted. (c) The time-dependent electron density in the conduction band $\rho_c(k,t)$. Γ and $\pm$M points are indicated on the right-hand vertical axis. The density is in linear scale shown along the vertical axis on the left. (d) The k-dependent TDP along the $\Gamma-$M direction (x direction). The largest difference in TDP ($\Delta\theta$) that an electron orbit can yield is about 0.07π. The laser parameters are 2000 nm in wavelength, 25 fs in FWHM and 2×10^{12} W/cm^2 in intensity.

closely related to $g(\mathbf{k})$ and $f(\mathbf{k})$, which in turn are determined by the spatial structure of the crystal. Can the even harmonics be enhanced by changing the lattice separation? If the answer is yes, then even harmonics may provide a simple means for probing the strain of a gapped graphene. In particular, due to the femtosecond nature of the driving lasers, HHG may be used to probe the lattice dynamics at femtosecond timescale. In this exploratory study, we calculated the generation of even harmonics by changing the bond length $|\mathbf{R}_1|$ of the gapped graphene, while $|\mathbf{R}_2|$ and $|\mathbf{R}_3|$ are kept fixed. Consider a highly deformed gapped graphene with $|\mathbf{R}_1|$=0.71 Å, and $|\mathbf{R}_2|$=$|\mathbf{R}_3|$=1.42 Å, its real space and reciprocal space structure are shown in Figs. 5(a) and (b). The most important difference between the normal and the deformed gapped graphene lies in their TDPs which are presented in Fig. 5(c), from which one can see that the maximum $\Delta\theta$ that an electron orbit can accumulate between ionization and recombination is increased to about 0.15π. Based on the earlier analysis, the increase of $\Delta\theta$ would result in an enhancement of even harmonics. In Fig. 6, the harmonic spectrum from the deformed gapped graphene (red solid line) is compared to the spectrum from the normal one (black dashed line). As expected, the efficiency of even harmonics is greatly increased in the deformed gapped graphene. To emphasize the role of TDP, we

also calculated the harmonic spectrum from the deformed gapped graphene but kept the TDP unchanged (i.e., the TDP corresponding to $|\mathbf{R}_1| = 1.42$ Å). As shown in the blue short dashed lines in Fig. 6, when the TDP is fixed, the efficiency of even harmonics cannot be increased.
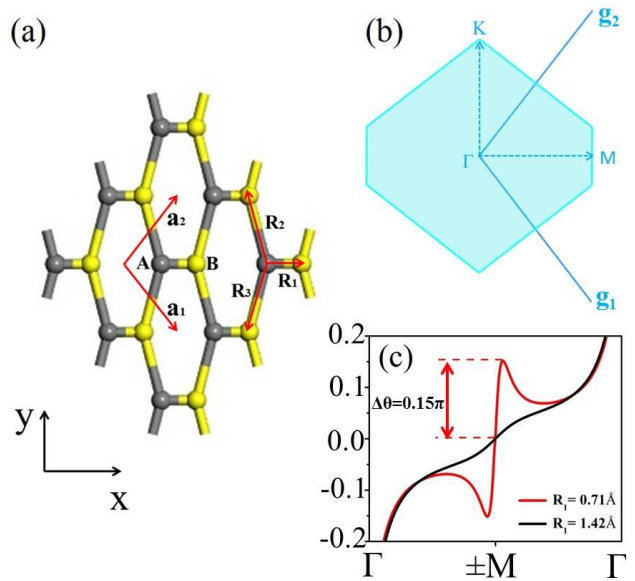

FIG. 5. (a) The real space structure of a deformed gapped graphene with $|\mathbf{R}_1|$=0.71 Å and $|\mathbf{R}_2|$ = $|\mathbf{R}_3|$=1.42 Å. (b)The reciprocal space of the deformed gapped graphene . $\mathbf{g_i}$ is the reciprocal lattice vector. High symmetry points, Γ, M and K, are labeled. (c) Comparison between the TDP for normal gapped graphene ($|\mathbf{R}_1|$=1.42 Å) and deformed gapped graphene ($|\mathbf{R}_1|$=0.71 Å).

The change of lattice separation in the example above is quite large. The example was used to demonstrate that even harmonics may become as strong as the odd harmonics when symmetry is broken. In Fig. 7(a) we show the TDPs vs small increment of the bond length $|\mathbf{R}_1|$ with the other two fixed. We can see that the TDP is very sensitive to $|\mathbf{R}_1|$ and the maximum $\Delta\theta$ is shown to increase rapidly as $|\mathbf{R}_1|$ is decreased from 1.42 Å to 0.71 Å, resulting in higher efficiency in the generation of even harmonics, as shown in Fig. 7(b). For smaller lattice change, we examine the growth of even harmonics when $|\mathbf{R}_1|$ is compressed gradually till to about 20 % smaller. In Fig. 7(c), we observe that the 2nd and 4th harmonics are only gradually enhanced within a change of $|\mathbf{R}_1|$ of less than 10%. Only for a change of above 10% the even harmonics are beginning to increase more rapidly. Without extensive investigations on more systems, it is difficult to draw conclusions whether the even harmonics would rise rapidly when the lattice constants are compressed or stretched from the equilibrium position. If it does, certainly measuring the change of the growth of even harmonics would serve a great potential for probing the deformation of lattice constants in a crystal with femtoseconds temporal resolution of the lasers. We note
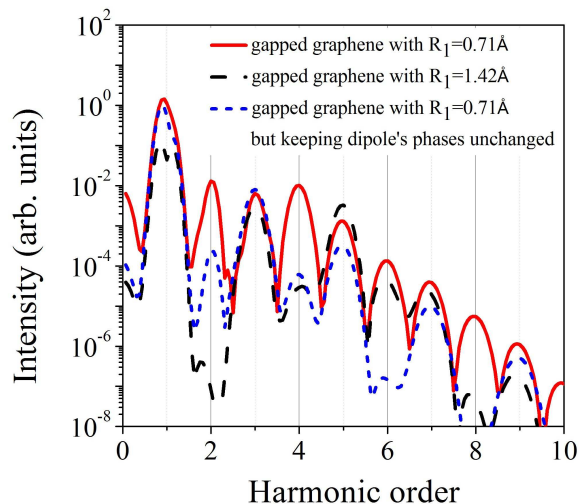
FIG. 6. The black (dark) dashed line is the harmonic spectrum from the normal gapped graphene. The red (gray) solid line is the harmonic spectrum from the deformed gapped graphene. The blue (short dashed) line is the harmonic spectrum from deformed gapped graphene, but the TDP is kept unchanged. The laser is polarized along the $\Gamma-M$ direction (x direction). Laser parameters are: 10 fs in FWHM, 800 nm in wavelength and 2×10^{12} W/cm^2 in intensity.

that in many solids the strain can be about 2% in experiments [41–43], but for a dynamic system larger strains can be expected. A number of theoretical papers have studied strains reaching 30% recently [36, 44–46].

VI. SUMMARY

In this work we established the important role of the transition dipole phase (TDP) in high-order harmonic generation from solids. The TDP has been disregarded in almost all of the previous theoretical studies. We showed that TDP can be ignored and only odd harmonics will appear if the crystal possesses inversion symmetry. This property can be generalized to systems with reflection symmetry. If the crystal has reflection symmetry with respect to the plane perpendicular to the laser polarization direction, then the TDP of the parallel component of the transition dipole can also be ignored and only odd harmonics will appear in the parallel polarization. Without the aforementioned spatial symmetry, the TDP cannot be ignored and even and odd harmonics are expected to appear simultaneously. In the present study, even harmonics reflect the symmetry property of the crystal, rather than by the effect of contributions from multiple energy bands as purported previously. While the HHG spectra from graphene and gapped graphene are calculated theoretically under the tight-binding approximation in the two-band model, we believe that more extensive calculations would improve but not negate the conclusion
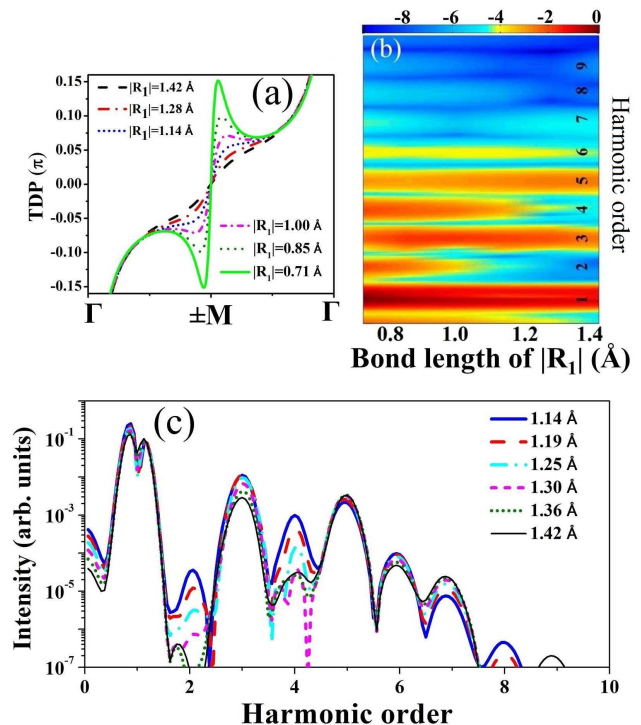

FIG. 7. (a) The dependence of the TDP from $\Gamma-M$ on $|\mathbf{R}_1|$. (b) High-order harmonic spectra from deformed gapped graphene by varying $|\mathbf{R}_1|$ from 1.42 Å to 1.14 Å. The 1.14 Å corresponds to about 20% strain. (c) A overview of the change of harmonic spectra with different bond length. The laser is polarized along the $\Gamma-M$ direction, with laser parameters: 800 nm in wavelength, 2×10^{12} W/cm^2 in intensity and 10 fs in FWHM duration.

presented above. We have also shown that the strength of even harmonics depends on the variation of TDP from excitation to recombination. As the bond length is tuned the TDP is varied. This leads to the dependence of the ratio of the strength of even over odd harmonics on the geometry and size of the unit cell of a crystal. Further quantitative investigations of these observations would shed new lights on probing the structure information of crystals using the HHG spectroscopy.

is also supported by NSF of China (Grant No. 11704187).

APPENDIX A

In this Appendix we derive the semiconductor Bloch equations (SBEs) from TDSE in the length gauge. If the velocity gauge is used it would lead to divergence when the frequency of the laser approaches zero. Within the single-electron approximation the TDSE is

$$i\frac{\partial}{\partial t}\psi(\mathbf{r},t) = \left(\frac{\mathbf{p}^2}{2} + V(\mathbf{r}) + \mathbf{r}\cdot\mathbf{F}(t)\right)\psi(\mathbf{r},t). \quad (A1)$$

By using the field-free Bloch functions as the basis set, the wavefunction $\psi(\mathbf{r},t)$ can be expanded as

$$\psi(\mathbf{r},t) = \sum_m \int_{BZ} d\mathbf{k}\, a_m(\mathbf{k},t)\phi_{m,\mathbf{k}}(\mathbf{r}), \quad (A2)$$

with $\phi_{m,\mathbf{k}}(\mathbf{r}) = \frac{1}{\sqrt{N}}u_{m,\mathbf{k}}(\mathbf{r})e^{i\mathbf{k}\cdot\mathbf{r}}$. Here $u_{m\mathbf{k}}(\mathbf{r})$ is the periodical part of the Bloch function. N is the number of unit cells in the crystal. The wavefunctions $\phi_{m,\mathbf{k}}(\mathbf{r})$ form a complete and orthonormal basis set

$$\int_{crystal}\phi_{m,\mathbf{k}}^*(\mathbf{r})\phi_{m'\mathbf{k}'}(\mathbf{r})dr = \delta_{m,m'}\delta_{\mathbf{k},\mathbf{k}'}. \quad (A3)$$

By inserting Eq. (A2) into Eq. (A1), multiplying $\phi_{m',\mathbf{k}'}^*(\mathbf{r})$ and integrating this equation over the real space, Eq. (A1) becomes

$$i\frac{\partial}{\partial t}a_m(\mathbf{k},t) = E_m(\mathbf{k})a_m(\mathbf{k},t)$$
$$+ \mathbf{F}(t)\cdot\sum_{m'}\int_{BZ} d\mathbf{k}'\, a_{m'}(\mathbf{k}',t)\xi(m,m',\mathbf{k},\mathbf{k}'), \quad (A4)$$

where

$$\xi(m,m',\mathbf{k},\mathbf{k}') = \frac{1}{N}\int_{crystal} u_{m,\mathbf{k}}^*(\mathbf{r})\mathbf{r}u_{m',\mathbf{k}'}(\mathbf{r})e^{i(\mathbf{k}'-\mathbf{k})\cdot\mathbf{r}}d\mathbf{r}. \quad (A5)$$

The most troublesome object is the transition dipole term $\xi(m,m',\mathbf{k},\mathbf{k}')$. To deal with this integral, in the first approach one would break the integration in Eq. (A5) to a sum of integrals over each unit cell

$$\xi(m,m',\mathbf{k},\mathbf{k}') = \delta_{\mathbf{k},\mathbf{k}'}\int_{cell} u_{m,\mathbf{k}}^*(\mathbf{r})\mathbf{r}u_{m',\mathbf{k}'}(\mathbf{r})dr$$
$$+ \frac{1}{N}\sum_{n=0}^{N-1} n\mathbf{R}e^{in(\mathbf{k}'-\mathbf{k})\cdot\mathbf{R}}\int_{cell} u_{m,\mathbf{k}}^*(\mathbf{r})u_{m',\mathbf{k}'}(\mathbf{r})e^{i(\mathbf{k}'-\mathbf{k})\cdot\mathbf{r}}d\mathbf{r}. \quad (A6)$$

The first term on the right-hand side depends on the choice of the unit cell. Thus, this is not an effective method.

The second approach to the infinite integration in Eq. (A5) is to translate the real space into reciprocal space representation. Because

$$\nabla_{\mathbf{k}}\left(u_{m,\mathbf{k}}(\mathbf{r})e^{i\mathbf{k}\cdot\mathbf{r}}\right) = e^{i\mathbf{k}\cdot\mathbf{r}}\nabla_{\mathbf{k}}u_{m,\mathbf{k}}(\mathbf{r}) + i\mathbf{r}u_{m,\mathbf{k}}(\mathbf{r})e^{i\mathbf{k}\cdot\mathbf{r}}, \quad (A7)$$

we can get

$$\mathbf{r}u_{m,\mathbf{k}}(\mathbf{r})e^{i\mathbf{k}\cdot\mathbf{r}} = -i\nabla_{\mathbf{k}}\left(u_{m,\mathbf{k}}(\mathbf{r})e^{i\mathbf{k}\cdot\mathbf{r}}\right) + ie^{i\mathbf{k}\cdot\mathbf{r}}\nabla_{\mathbf{k}}u_{m,\mathbf{k}}(\mathbf{r}). \quad (A8)$$

Using the relationship Eq. (A8) we can rewrite Eq. (A5) as

$$\xi(m,m',\mathbf{k},\mathbf{k}') = -i\delta_{m,m'}\nabla_{\mathbf{k}'}\delta_{\mathbf{k},\mathbf{k}'}$$
$$+ i\frac{1}{N}\int_{crystal} u_{m,\mathbf{k}}^*(\mathbf{r})e^{i(\mathbf{k}'-\mathbf{k})\cdot\mathbf{r}}\nabla_{\mathbf{k}'}u_{m',\mathbf{k}'}(\mathbf{r})d\mathbf{r}. \quad (A9)$$

The second term on the right hand side of Eq. (A9) still contains an integration over the whole crystal. We can constrain this integration within the unit cell

$$\frac{1}{N}\int_{crystal} u_{m,\mathbf{k}}^*(\mathbf{r})e^{i(\mathbf{k}'-\mathbf{k})\cdot\mathbf{r}}\nabla_{\mathbf{k}'}u_{m',\mathbf{k}'}(\mathbf{r})d\mathbf{r}$$
$$= \sum_{n=0}^{N-1}\frac{1}{N}e^{in(\mathbf{k}'-\mathbf{k})\cdot\mathbf{R}}\int_{cell} u_{m,\mathbf{k}}^*(\mathbf{r})e^{i(\mathbf{k}'-\mathbf{k})\cdot\mathbf{r}}\nabla_{\mathbf{k}'}u_{m',\mathbf{k}'}(\mathbf{r})d\mathbf{r}. \quad (A10)$$

Because $\sum_{n=0}^{N-1}\frac{1}{N}e^{in(\mathbf{k}'-\mathbf{k})\cdot\mathbf{R}} = \delta_{\mathbf{k},\mathbf{k}'}$, the expression Eq. (A10) is equivalent to

$$\delta_{\mathbf{k},\mathbf{k}'}\int_{cell} u_{m,\mathbf{k}}^*(\mathbf{r})\nabla_{\mathbf{k}}u_{m',\mathbf{k}}(\mathbf{r})d\mathbf{r}. \quad (A11)$$

Using Eq. (A11), Eq. (A9) can be rewritten as

$$\xi(m,m',\mathbf{k},\mathbf{k}') = -i\delta_{m,m'}\nabla_{\mathbf{k}'}\delta_{\mathbf{k},\mathbf{k}'}$$
$$+ i\delta_{\mathbf{k},\mathbf{k}'}\int_{cell} u_{m,\mathbf{k}}^*(\mathbf{r})\nabla_{\mathbf{k}}u_{m',\mathbf{k}}(\mathbf{r})d\mathbf{r}. \quad (A12)$$

Then, by inserting Eq. (A12) into Eq. (A4), we can get

$$i\frac{\partial}{\partial t}a_m(\mathbf{k},t) = E_m(\mathbf{k})a_m(\mathbf{k},t)$$
$$- i\mathbf{F}(t)\cdot\int_{BZ} a_m(\mathbf{k}',t)\nabla_{\mathbf{k}'}\delta_{\mathbf{k},\mathbf{k}'}d\mathbf{k}'$$
$$+ \mathbf{F}(t)\cdot\sum_{m'}\int_{BZ} a_{m'}(\mathbf{k},t)\mathbf{D}(m,m',\mathbf{k})d\mathbf{k}, \quad (A13)$$

where $\mathbf{D}(m,m',\mathbf{k}) = i\int_{cell} u_{m,\mathbf{k}}^*(\mathbf{r})\nabla_{\mathbf{k}}u_{m',\mathbf{k}}(\mathbf{r})d\mathbf{r}$.

According to the Gauss theorem,

$$
\int\limits_{BZ} a_m(\mathbf{k}',t)\nabla_{\mathbf{k}'}\delta_{\mathbf{k},\mathbf{k}'}d\mathbf{k}'
$$
$$
= \int\limits_{S} a_m(\mathbf{k}',t)\delta_{\mathbf{k},\mathbf{k}'}\hat{\sigma}dS' - \int\limits_{BZ} \delta_{\mathbf{k},\mathbf{k}'}\nabla_{\mathbf{k}'}a_m(\mathbf{k}',t)d\mathbf{k}'
$$
$$(A14)$$

The first term on the right hand side of Eq. (A14) is a surface integral over the surface of the Brillouin zone. $\hat{\sigma}$ is the normal unit vector of the surface. Since there is no discontinuous points in the Brillouin zone, this term can be dropped. Equation (A13) then becomes

$$
\frac{\partial}{\partial t}a_m(\mathbf{k},t) = -iE_m(\mathbf{k})a_m(\mathbf{k},t) + \mathbf{F}(t)\cdot\nabla_{\mathbf{k}}a_m(\mathbf{k},t)
$$
$$
- i\mathbf{F}(t)\cdot\sum_{m'}a_{m'}(\mathbf{k},t)\mathbf{D}(m,m',\mathbf{k}). \quad (A15)
$$

Introducing the micropolarization $p_{mn}(\mathbf{k},t) = a_m(\mathbf{k},t)a_n^*(\mathbf{k},t)$ and the electron density $\rho_m(\mathbf{k},t) = |a_m(\mathbf{k},t)|^2$, for the two bands consisting of a conduction band and a valence band, Eq. (A15) then lead to the SBEs:

$$
\frac{\partial}{\partial t}p_{cv}(\mathbf{k},t) = -i[E_c(\mathbf{k})-E_v(\mathbf{k})]p_{cv}(\mathbf{k},t) + \mathbf{F}(t)\cdot\nabla_{\mathbf{k}}p_{cv}(\mathbf{k},t)
$$
$$
+ i\mathbf{F}(t)\cdot\mathbf{D}_{cv}(\mathbf{k})[\rho_c(\mathbf{k},t)-\rho_v(\mathbf{k},t)],
$$
$$(A16)$$
$$
\frac{\partial}{\partial t}\rho_v(\mathbf{k},t) = -2\mathrm{Imag}[\mathbf{F}(t)\cdot\mathbf{D}_{cv}(\mathbf{k})p_{cv}(\mathbf{k},t)]
$$
$$
+ \mathbf{F}(t)\cdot\nabla_{\mathbf{k}}\rho_v(\mathbf{k},t), \quad (A17)
$$
$$
\frac{\partial}{\partial t}\rho_c(\mathbf{k},t) = 2\mathrm{Imag}[\mathbf{F}(t)\cdot\mathbf{D}_{cv}(\mathbf{k})p_{cv}(\mathbf{k},t)]
$$
$$
+ \mathbf{F}(t)\cdot\nabla_{\mathbf{k}}\rho_c(\mathbf{k},t). \quad (A18)
$$

APPENDIX B

In this Appendix, we analyze the influence of TDP on the intraband harmonics. For the intraband transitions, it is not as straightforward to obtain an obvious relationship between the TDP and the efficiency of N_{th}-order harmonic like equation (35) for interband transitions. Because of the four-fold integrations in equation (31), there is no quantum orbits for intraband HHG process. Nevertheless we still can find relationship between intraband harmonics and TDPs. From equation (31), saddle point approximation can be applied to the integration for $\mathbf{k}$, t', t'' and t. Similar to the interband case, there always exist two events,(k_s,t_s,t_s',t_s'') and $(-k_s,t_s+T/2,t_s'+T/2,t_s''+T/2)$ over one optical cycle. What one should be warned about is that the word "event" is used here instead of "trajectory" because there is no quantum orbit for intraband process. If we define $D_{cv}(k_s,t_s',t_s) = D_{cv}(k_s+A(t_s)-A(t_s'))$, under the conditions of $\mathbf{v}(\mathbf{k})=-\mathbf{v}(-\mathbf{k})$, $F(t)=-F(t+T/2)$, and $A(t)=-A(t+T/2)$, the contribution from these two events to the N_{th} order harmonic is proportional to

$$
\Delta_N = \sum_{\lambda=c,v}\mathbf{v}_\lambda(k_s)F(t_s')F(t_s'')
$$
$$
\times\{e^{-iN\omega_0 t_s}D_{cv}^*(k_s,t_s',t_s)D_{cv}(k_s,t_s'',t_s)
$$
$$
- e^{-iN\omega_0 t_s-iN\pi}D_{cv}(k_s,t_s',t_s)D_{cv}^*(k_s,t_s'',t_s)\}.
$$
$$(A19)$$

Then, one can get

$$
\Delta_N \sim e^{i\{\theta(k_s,t_s'',t_s)-\theta(k_s,t_s',t_s)\}} - e^{-i\{\theta(k_s,t_s'',t_s)-\theta(k_s,t_s',t_s)\}}e^{-iN\pi},
$$
$$(A20)$$

which is similar to Eq. (35). This means the relationship between the efficiency of even harmonics from intraband component and TDP behaves just like the interband case. If the system possesses symmetry such that Eq. (18) holds, then Δ_N is proportional to $(1-e^{-iN\pi})$, which is similar to the interband components. As a result, there is no even harmonics. Once the symmetry is broken, even harmonics come into appearance.

[1] S. Ghimire, A. D. DiChiara, E. Sistrunk, P. Agostini, L. F. DiMauro, and D. A. Reis, Nat. Phys. **7**, 138 (2011).
[2] G. Ndabashimiye, S. Ghimire, M. Wu, D. A. Browne, K. J. Schafer, M. B. Gaarde, and D. A. Reis, Nature **534**, 520 (2016).
[3] T. T. Luu, M. Garg, S. Yu. Kruchinin, A. Moulet, M. Th. Hassan, and E. Goulielmakis, Nature **521**, 498 (2015).
[4] Ghimire, Shambhu, J. Phys. B: At. Mol. Opt. Phys. **47**, 204030 (2014).
[5] M. Schultze et al., Nature **493**, 75 (2013).
[6] A. Schiffrin et al., Nature **493**, 70 (2013).
[7] G. Vampa et al., Phys. Rev. Lett. **115**, 193603 (2015).
[8] C. M. Wang, T. S. Ho, and S. I. Chu, J. Phys. B: At. Mol. Opt. Phys. **49**, 225401 (2016).
[9] A. A. Lanin, E. A. Stepanov, A. B. Fedotov, and A. M. Zheltikov, Optica, **4**, 516 (2017).
[10] Y. S. You, D. A. Reis, and S. Ghimire, Nat. Phys. **13**, 345 (2017).
[11] E. N. Osika et al., Phys. Rev. X, **7**, 021017 (2017).
[12] M. X. Wu, S. Ghimire, D. A. Reis, K. J. Schafer, and M. B. Gaarde, Phys. Rev. A **91**, 043839 (2015).

[13] M. Korbman, S. Y. Kruchinin, and V. S. Yakovlev, New Journal of Physics **15**, 013006 (2013).

[14] N. Tancogne-Dejean, O. D. Mücke, F. X. Kärtner, and A. Rubio, Phys. Rev. Lett. **118**, 087403 (2017).

[15] G. Wachter, C. Lemell, J. Burgdörfer, S. A. Sato, X. M. Tong, and K. Yabana, Phys. Rev. Lett. **113**, 087401 (2014).

[16] I. Floss, *et al.*, arXiv preprint arXiv:1705.10707 (2017).

[17] D. Golde, T. Meier, and S. W. Koch, J. Opt. Soc. Am. B **23**, 2559 (2006)

[18] D. Golde, T. Meier, and S. W. Koch, Phys. Rev. B **77**, 075330 (2008).

[19] P. Földi, M. G. Benedict, and V. S. Yakovlev, New J. Phys. **15**, 063019 (2013).

[20] O. Schubert *et al.*, Nat. Photonics **8**, 119 (2014).

[21] S. C. Jiang, C. Yu, G. L. Yuan, T. Wu, Z. W. Wang, and R. F. Lu, J. Phys.: Condens. Matter **29**, 275702 (2017).

[22] M. Hohenleutner, F. Langer, O. Schubert,M. Knorr, U. Huttner, S.W. Koch, M. Kira, and R. Huber, Nature (London) **523**, 572 (2015).

[23] F. Langer et al., Nature **533**, 7602 (2016).

[24] C. Yu, X. R. Zhang, S. C. Jiang, X. Cao, G. L. Yuan, T. Wu, L. H. Bai, and R. F. Lu, Phys. Rev. A **94**, 013846 (2016).

[25] S. G. Mirzaei, J. Beetar, and M. Chini, Appl. Phys. Lett. **110**, 061101 (2017).

[26] H. Liu, Y. Li, Y. S. You, S. Ghimire, T. F. Heinz, and D. A. Reis, Nat. Phys. **13**, 262 (2016).

[27] F. Langer, M. Hohenleutner, U. Huttner, S. W. Koch, M. Kira, and R. Huber, Nat. Photonics **11**, 227 (2017).

[28] T. T. Luu, and H. J. Wörner, Phys. Rev. B **94**,115164 (2016).

[29] M. S. Wismer, S. Y. Kruchinin, M. Ciappina, M. I. Stockman, and V. S. Yakovlev, Phys. Rev. Lett. **116**, 197401 (2016).

[30] H. K. Kelardeh, V. Apalkov, and M. I. Stockman, Phys. Rev. B **92**, 045413 (2015).

[31] H. K. Kelardeh, V. Apalkov, and M. I. Stockman, Phys. Rev. B **91**, 045493 (2015).

[32] I. Al-Naib, J. E. Sipe, and M. M. Dignam, Phys. Rev. B **90**, 245423 (2014).

[33] D. Dimitrovsk, L. B. Madsen, and G. Pedersen, Phys. Rev. B **95**, 035405 (2017).

[34] N. Yoshikawa, T. Tamaya, and K. Tanaka, Science **356**, 736 (2017).

[35] R. Saito, G. Dresselahus, M.S. Dresselhaus, Physical Properties of Carbon Nanotubes, Imperial College Press, 1998.

[36] G. Gui, J. Li, and J. X. Zhong, Phys. Rev. B **78**, 075435 (2008).

[37] G. Vampa, C. R. McDonald, G. Orlando, D. D. Klug, P. B. Corkum, and T. Brabec, Phys. Rev. Lett. **113**, 073901 (2014).

[38] G. Vampa, C. R. McDonald, G. Orlando, P. B. Corkum, and T. Brabec, Phys. Rev. B **91**, 064302 (2015).

[39] M . Lewenstein, Ph. Balcou, M. Yu. Ivanov, A. L'Huillier, and P. B. Corkum, Phys. Rev. A **49**, 2117 (1994).

[40] V. M. Pereira, A. C. Neto, and N. M. R. Peres, Phys. Rev.B,**80**, 045401 (2009).

[41] T. M. G. Mohiuddin et al. Phys. Rev. B **79** 205433 (2009).

[42] Z. Ni, H. M. Wang, Y. Ma, J. Kasim, Y. H. Wu, and Z. X. Shen, ACS Nano **2**, 1033 (2008).

[43] G. Tsoukleri, et al., Small **5**, 2397 (2009).

[44] V. M. Pereira, A. H. Castro Neto, and N. M. R. Peres, Phys. Rev. B **80**, 045401 (2009).

[45] F. M. D. Pellegrino, G. G. N. Angilella, and R. Pucci, Phys. Rev. B **81**, 035411 (2010).

[46] S. M. Choi, S. H. Jhi, and Y. W. Son, Phys. Rev. B **81**, 081407 (2010).